A large-scale high-resolution numerical model for sea-ice fragmentation dynamics

Jan Åström[1], Fredrik Robertsen[1], Jari Haapala[2], Arttu Polojärvi[3], Rivo Uiboupin[4], and Ilja Maljutenko[4]

[1]CSC – It center for science Ltd. P.O. Box 405 FI-02101 Espoo, Finland
[2]Finnish Meteorologìcal Institute, Helsinki, Finland
[3]Aalto University, School of Engineering, Department of Mechanical Engineering, P.O. Box 14100, FI-00076 Aalto, Finland
[4]Tallinn University of Technology, Department of Marine Systems, Akadeemia tee 15a, Tallinn 12618, Estonia

Correspondence: astrom@csc.fi

Abstract. Sea ice motion and fragmentation forecasts are of vital importance for all human interaction with sea ice, ranging from indigenous hunters to shipping in polar regions. Sea ice models are also important for modelling long term changes in a warming climate. Here we apply a discrete element model (HiDEM), originally developed for glacier calving, to sea ice break-up and dynamics. The code is highly optimized to utilize high-end supercomputers to achieve extreme time and space resolution. Simulated fracture patterns and ice motion are compared to satellite images in the Kvarken region of the Baltic Sea in March 2018. A second application is ice ridge formation in the ~~Bay~~ Gulf of Riga. With a few tens of graphics processing units (GPUs) the code is capable of reproducing observed ice patterns, that in nature may take a few days to form, over an area $\sim 100km \times 100km$, with an $8m$ resolution, in computations lasting ~ 10 hours. The simulations largely reproduce observed fracture patterns, ice motion, fast ice regions, floe size distributions, and ridge patterns. The similarities and differences between observed and computed ice dynamics and their relation to initial conditions, boundary conditions and applied driving forces are discussed in detail. The results reported here indicate that HiDEM has the potential to be developed into a high-resolution detailed model for sea ice dynamics over short time scales, which combined with large-scale and long-term continuum models may form an efficient framework for sea ice dynamics forecasts.

1 Introduction

Reliable forecast models for ice dynamics are of vital importance for all human activities related to sea ice. Indigenous hunters in the Arctic can move fast over long distances across level landfast ice, while travelling on drift ice or on land can be immensely more difficult. Similarly, sustainable and safe winter navigation is dependent on ice conditions, with constant route optimizations to avoid packed or ridged ice. Sea ice also plays a major role in the design of offshore structures, such as wind turbines, and in cold regions sea ice may be a hindering factor for renewable energy. In addition, large scale implementation of offshore wind farms may affect local sea ice dynamics. For all of these purposes, new high resolution ice models capable of modelling ice dynamics across tens to hundreds of kilometers are needed.

Traditionally, large scale continuum models have been used for modelling sea ice dynamics on scales larger than kilometers. Such models are computationally efficient, and can easily be extended over larger areas and longer times compared to the

discrete element method (DEM) approach used here. A well known challenge with continuum models is that an effective rheology for sea ice has to be implemented in the model, and there is no easy and straight-forward way to model all necessary aspects of sea ice dynamics with a large scale effective rheology. Some of the early attempts in this direction was the visco-plastic model (Hibler, 1977; 1979) developed already in the 1970's. The visco-plastic model by Hibler can capture some large scale effective ice dynamics, but fails to model formation of leads, compression ridges, shear zones and floe fields that are obvious on scales smaller than $\sim 100km$. ~~Much more elaborate and~~ More advanced and more accurate continuum models are e.g. the elastic-decohesive model of Schreyer et al. (2006) and the Maxwell elasto-brittle model by Dansereau et al. (2016) and the brittle Bingham-Maxwell rheology model by Olasson et al. (2022). Several modern high resolution continuum models are able to capture many of the characteristics of large scale fracturing (Bouchat et al. (2022); Hutter et al. (2022)), and some are even utilized as operational applications tools with a few kilometers grid resolution (Pemberton et al. (2017); Kärnä et al. (2021); Röhrs et al. (2023)). However, even advanced and modern continuum models struggle with modelling detailed ice structures such as leads and ridges.

DEM models take a significantly different approach. Instead of modeling sea ice as a continuum, solid and elastic blocks are initially connected together to form sea-ice. The dynamics is typically computed via discrete versions of Newtons equations with some sort of energy dissipation terms. When load is applied, the connections may break, and ice disintegrates into discrete floes. Early models of this kind utilized circular ~~DEs~~ Discrete Elements (DEs) moving in two dimensions (Babic et al. (1990); Hopkins and Hibler (1991); Blockley (2020)). Hopkins and Thorndike (2006) modeled Arctic pack ice using a DE-model. The resolution of these models were not enough to resolve details, instead important features, such as ridging, were described by an ice floe interaction model. A similar approach was later adopted by West et al. (2022) ~~and Damsgaard (2021, 2018)~~ who simulated ice dynamics in the Nares strait, and by Damsgaard (2021, 2018) investigating pressure ridging. Also a recent investigation by Manucharyan and Montemuro (2022), introducing complex discrete elements with time-evolving shapes, relied on a similar approach. In addition, they used a rudimentary failure model to describe the failure of sea ice. Our model is not related to these models, instead we explicitly model ice dynamics at a few-meters scale, including ridging, leads, shear and tensile fractures, with the large-scale ice failure patterns emerging as collective results of these smaller scale failure processes. Neither does our model rely on an assumption of ice floes, but instead we let the ice floes form and fracture throughout the simulations.

The objecive of this investigation is to bridge some of the gaps between continuum models and DE-models by implementing and testing a computationally efficient DEM that has been developed and optimised for high-end computers with wast numbers of the most efficient processors currently available. If a detailed high-fidelity model of this kind can be scaled up to length scales at which continuum models are sufficient and then the two can be combined into a unified framework, a very useful forecast model for sea ice dynamics may be the result.

2 The HiDEM model for sea ice

2.1 Mechanics of HiDEM

The algorithm of the HiDEM code is a discrete element model. A DEM formulation for sea ice motion can be related to the Cauchy momentum equation (Acheson (1990)), which treats sea ice as a continuum. In its full form, this equation accounts for coriolis force, atmospheric and ocean stresses, sea surface tilt and Cauchy stresses within pack ice. The Cauchy momentum equation reads

$$m\left(\frac{D\boldsymbol{u}}{Dt} + f\boldsymbol{k}\times\boldsymbol{u}\right) = \boldsymbol{\tau}^a + \boldsymbol{\tau}^w + m\boldsymbol{g}\Delta H + \boldsymbol{\nabla}\cdot\boldsymbol{\sigma}, \tag{1}$$

where m is the ice and snow mass, $\boldsymbol{u}$ is the horizontal ice velocity vector, f is the coriolis parameter, $\boldsymbol{k}$ is the upward unit vector, $\boldsymbol{\tau}^a$ and $\boldsymbol{\tau}^w$ are the stresses applied by air and water drag, $\boldsymbol{g}$ is the gravitational acceleration, ΔH is the vertical component of the sea surface tilt, and σ is the Cauchy stress tensor of ice.

Below we focus on short term sea ice deformations driven by the external forcing and modified by the coastal boundary conditions and sea ice fracturing. In this case, we can neglect the coriolis term and the sea surface tilt, after which the previous equation becomes

$$m\frac{D\boldsymbol{u}}{Dt} = \boldsymbol{\tau}^a + \boldsymbol{\tau}^w + \nabla\cdot\boldsymbol{\sigma}. \tag{2}$$

Assuming a simple linear Kelvin-Voigt type of viscoelasticity (Meyers et al. (2009)) the stress tensor for sea ice can be written as,

$$\boldsymbol{\sigma} = A\dot{\boldsymbol{\epsilon}} + B(\boldsymbol{x},t)\boldsymbol{\epsilon}, \tag{3}$$

where A represent dissipative deformations like viscosity, and $B(\boldsymbol{x},t)$ represent spatially and temporally varying brittle elasticity. Here, $\boldsymbol{\sigma}$ is stress and $\dot{\boldsymbol{\epsilon}}$ is strain rate.

DEM algorithms do not explicitly solve continuum equations, but instead resolve forces on interacting ~~discrete elements (DEs)~~DEs. The continuum equations above can be reformulated in a format more suitable for a DEM implementation. DEs interact pairwise either through beams connecting them or through repulsive contact forces. If we define the discrete position vector, x_i, of the DE i, which include three translational and three rotational degrees of freedom, the DEM equations of motions can be written as

$$m_i\ddot{\boldsymbol{x}}_i + \sum_j K\boldsymbol{x}_{ij} + \sum_j C_2\dot{\boldsymbol{x}}_{ij} + C_1\dot{\boldsymbol{x}}_i = \boldsymbol{F}_i, \tag{4}$$

where m_i is the mass or moment of inertia of i, C_1 is the drag coefficient of the combined drag of water and air, $\boldsymbol{F}_i$ are external forces and moments, such as gravity and buoyancy. Further, $K = K(t)$ and $C_2 = C(t)$ represent elements of contact stiffness and damping matrices for interacting discrete element pair i and j and $\boldsymbol{x}_{ij}$ refers to position vector between i and its neighbors j. $\ddot{x}$ and $\dot{x}$ are second and first time derivatives of x.K and C_2 correspond to B and A of Equation 3, respectively, and

Figure 1. In a DEM algorithm, an intact material is described by joining discrete elements (here of circular shape) by beams: (a) Tensile forces (F) break a beam connecting DEs if stretched beyond a limit, (b) Torque (T) also breaks a beam if difference in rotation angles is too large. (c) Discrete elements also interact through pairwise in-elastic collisions (Riikilä et al. (2015)).

depending on the pair of discrete elements, they may include either elements of stiffness and damping matrices of the beams or those related to repulsive contacts of the discrete elements.

In the previous equation, $\sum_j K\boldsymbol{x}_{ij} + \sum_j C_2\dot{\boldsymbol{x}}_{ij}$ corresponds to $\nabla \cdot \sigma$ in Equation 2, with the divergence operator being replaced by a sum over all of its neighbouring discrete elements of i. This can be done as the contact forces from neighbors on opposite sides of a discrete element cancel each other if they apply equal force on i and, thus, only change in the force across an element induces motion. Further, $C_1\dot{\boldsymbol{x}}_i$ and $\boldsymbol{F}_i$ of Equation 4 include the effect of stresses $\boldsymbol{\tau}^a$ and $\boldsymbol{\tau}^w$ in Equation 2. DEM simulations utilize explicit time stepping. For this, the previous equation can be written in discrete form by using the definition of derivatives, and the motion of the discrete elements ($\boldsymbol{x}(t+dt)$ as function of $\boldsymbol{x}(t)$ and $\boldsymbol{x}(t-dt)$) can be computed via iterations of time-steps (dt) based on element positions, velocities and forces acting on it.

2.2 Code optimization for High-Performance-Computing

Any computational implementation of Eq. (4) is a trade-off between accuracy and computational efficiency. ~~In the investigation here, the focus is~~ A higher accuracy would mean e.g. including irregular elements, higher-order time-integration schemes, non-linear elasticity and/or non-linear drag coefficients. In contrast, simpler models with a higher computational efficiency allows for a finer resolution. I.e. smaller elements and timesteps. The HiDEM code is focused on the latter~~as we use equal size spheres connected by breakable Euler-Bernoulli beams in close-packed configuration. While the approach chosen here is computationally optimal for DEM simulations, it introduces a weak anisotropy in the material stiffness and limits the crack propagation directions to a few preferred ones on the scale of a discrete element. This anisotropy is on the larger scale, however, easily broken as demonstrated by a snapshot of a HiDEM simulation (Fig. 2A.~~ The basic algorithm of HiDEM is fairly standard for this type of codes: A large set of elements that move relatively to each other and that interact only with neighbors within a limited maximum interaction range. A clear majority of the computational effort for algorithms of this kind has to be dedicated to computing forces between elements. With such a code structure HiDEM is a good candidate for efficient implementation on the most powerful modern high performance computers (HPC). The HiDEM code is written in C++ with MPI (Message Passing Interface) and OpenMP (Open Multi-Processing, version 4.x or higher) for parallelization and multithreading. Offloading to GPUs is done using Cuda/Hip. The code is optimized for maximum computational efficiency on supercomputers or large clusters with an efficient interconnect. The code can either be compiled for running only on CPUs or a combination of CPUs and GPUs with almost all computations taking place on the GPUs.

The HiDEM code has thus two levels of parallelization in two different ways: MPI message passing between CPU nodes, and OpenMP multithreading on CPUs with many compute cores, and, alternatively, MPI for CPUs and offloading the most compute intensive parts, using Cuda/Hip, to GPUs. This structure creates a high complexity of the code, and extreme care has

Figure 2. (*A*) The two simulation domains in Kvarken and the Gulf of Riga indicated by rectangles. (*B*) All DEs displayed in a $\sim 10km \times 7km$ area in the south-western corner of the Kvarken simulation domain at a late stage of the 8/3/18 simulation when the ice is broken up. The straight boundary, from east to west, between drift and, initially stronger, landfast ice is indicated in the figure.

been taken to implement optimal data structures and communications so that the compute power of the GPUs can be utilized as efficiently as possible. The technical details of the codes data structures and communication schemes are outside the scope of this article and will be reported elsewhere.

The results reported here were run on the LUMI supercomputer in Kajaani, Finland. In June 2023 LUMI was ranked third on the top500-list of the world's fastest supercomputers. The LUMI GPU-partition has 2928 GPU nodes each with a 64 core CPU and 8 Graphics Compute Dies (GCDs). For ~~this simulation~~ the results reported here we performed runs with about 100 million elements with roughly half a billion interactions, and a few million time steps. A simulation lasted typically about 10-20 hours, and we used no more than 4 GPU-nodes which means there is still a lot of potential to scale up both element count and to increase time integration speed. The extreme computational efficiency of the HiDEM code implemented in a suitable HPC environment, allowing for extreme scale and resolution properties, is what sets HiDEM apart from standard DEMs. DEM results cited in the Introduction above, typically report models with the order of 10,~~a square shaped sea-ice sheet of size 10 km × 10 km was modelled by using DEs of 1m diameter and subjected to uniaxial compression. It can be seen that the ice failure in these simulations becomes concentrated in several shear zones where ice ridges form. Fig. 2B shows an aerial photograph of ice ridges from the Gulf of Bothnia in March 2011 for comparison~~000 elements or for some larger element numbers, significantly larger timesteps for km-size elements. The resolution of HiDEM is demonstrated in Fig. 2B which display about 1% of the Kvarken simulation domain.

~~(a) HiDEM simulation of a failure of a 10 km × 10 km square-shaped sea-ice sheet subjected to uniaxial compression. The sheet was modelled by using dense-packed single-layer $1m$ diameter spherical discrete elements. The ice sheet fails in shear and ice ridges are formed. (b) An aerial picture at $30m$ altitude of fractured ice with compression ridges in the Gulf of Bothnia after a storm in March 2011.~~

2.3 Sea ice simulations

The purpose of this investigation is to a apply a simple and computationally efficient DEM implementation, as described above, to simulate sea ice fragmentation and compare the result to observations. We apply the HiDEM code to ice failure in the Kvarken region of the Baltic Sea and to ridge formation in the Gulf of Riga (Fig. 2). The objective of this exercise is to investigate how well the model can mimic the ice dynamics in Kvarken which is a narrow strait that is often ice covered on its NE side, while the sea often remain largely open on its SW side, creating interesting dynamics when wind presses ice towards the Southwest. Our second objective is to test how well the model mimics formation of ice compression ridges in the Gulf of Riga under strong SW winds. This is a well-known problem for shipping in that region.

Table 1. HiDEM parameters used. Drag and friction terms are linear in velocity. Drag coefficients are small to allow swift dynamics. Land friction is high to hinder ice from sliding on land. Damping is small compared to the critical damping of a harmonic oscillator to allow sound waves to travel in the ice, but large enough to hinder build up of vibrational kinetic energy in the ice.

Young's modulus	$2 \times 10^9 N/m^2$
Fracture stress	$5 \times 10^{-4} N/m^2$
Fracture mode	tension + constant*(bending and torsion)
Ice density	$910 kg/m^3$
Water density	$1027 kg/m^3$
DE diameter	$8m$
Air drag	$1 Ns/m^3$
Water drag	$20 Ns/m^3$
Land friction	$10^6 Ns/m^3$
Damping/critical-damping	10^{-3}

We use close-packed spherical DEs, all of similar size, 8 meters in diameter, and connected by Euler-Bernoulli beams. ~~We apply the HiDEM code to ice failure in the Kvarken region of the Baltic Sea and to ridge formation in the Bay of Riga (Fig. 3A)~~A beam connect two center points of a DE. Each DE, and thereby also the endpoints of a beam, have 6 degrees of freedom: three translational, and three rotational. Beams connect all, or a fraction of randomly selected, nearest neighbors. The matrix K in Eq. (4) contains the stiffness elements (or spring constants) that relates forces and torques to beam deformation. The stiffness matrix of a single beam, and other details, are given in Åström et al. (2013). All relations between forces and deformations are linear up to a beam breaking point, which is determined by the beam deformations, either as an elastic energy criterion or as a maximum stress/strain criterion. Once a beam is broken it vanishes. I.e. the connection between the DE's is irreversibly broken, and the DE's can freely move apart but will continue to interact if they are pressed against each other. DEM parameters are listed in Table ~~1.~~

~~The sea ice~~ 1, and the element interactions are sketched in Fig. 1. The animation in the Supplementary Material demonstrate simulated ice dynamics in a small fraction ($\sim 0.3\%$) of the Kvarken domain so that details can be seen.

The typical winter sea-ice thickness in the Kvarken region is of the order of one meter, or less. It means an accurate ice thickness can only be described explicitly if the diameter of the spherical elements is ~~much smaller~~ no more than one meter~~and several layers of spheres are used~~. This would increase computational requirements immensely ~~. Here we use , instead,~~ compared to the 8-meter spheres we use for the large scale simulations below. The number of elements would have to be increased by a factor 8^2 to simulate the same domain. Instead, we use a single layer of DEs ~~for ice thickness and~~ in a close-packed configuration forming a triangular lattice of 8 meter spheres.

A consequence of the 8 meter diameter is that the model ice will be significantly thicker and stronger than the ice that appears naturally in the region. Ice fractures when stress build-up reaches the fracture threshold of the ice. When the ice breaks, stress is relaxed. In order to simulate this we can define a dimensionless parameter, R_{ss}, that is the ratio of stress to strength ~~for the~~

~~beams as a governing model parameter~~of the model ice, and tune the applied stress on the ice in the simulations so that that this ratio is approximately equal to unity. The stress-to-strength ratio of the model ice is given by

$$R_{ss} = \frac{h\, l_{DE}\, E_{ice}\, \epsilon_{frac}}{f_{DE}\, L_{domain}/l_{DE}}, \tag{5}$$

where h is ice thickness, l_{DE} is the horizontal dimension of the DEs, $E_{ice}\epsilon_{frac}$ is the ice fracture stress, f_{DE} is the force applied on each DE, and L_{domain}/l_{DE} is the relative resolution of the simulation domain. R_{ss} is of order one, as it should be, if we use: $h = 1$, $l_{DE} = 8$, a driving forces of the order of $100N$/DE, an ice fracture stress of order $10^5 N/m^2$, and $L_{domain}/l_{DE} \sim 10^4$. A benefit of increasing f_{DE}, keeping R_{ss} fixed, is that ice dynamics can be made a bit faster, and forecasts corresponding to longer times can be done with shorter simulations.

The triangular lattice structure introduces a weak anisotropy in the material stiffness and limits the crack propagation directions to a few preferred ones on the scale of a DE. The triangular lattice has three possible crack propagation directions with a 60 degrees angle between them. These angles are however not visible in the larger scale fracture patterns in e.g. Fig. 2B, which means, on a large scale the model behave predominantly isotropic, as it should.

In spite of the limitations, the lack of details in the initial and boundary conditions, driving forces, and the simplicity of the DEM implementation, the model is, as demonstrated below, able to capture a great deal of the large scale structures and small scale details of observed sea ice fragmentation and dynamics.

~~(A) The two simulation domains in Kvarken and the Bay of Riga indicated by rectangles. (B) All DEs displayed in a $\sim 10km \times 7km$ area in the south-western corner of the Kvarken simulation domain. The straight east - west feature dividing ice into broken and solid ice is a boundary between initially stronger fast-ice and initially more damaged ice, like partly refrozen ice-rubble.~~

~~HiDEM parameters used. Drag and friction terms are linear in velocity. Drag coefficients are small to allow swift dynamics. Land friction is high to hinder ice from sliding on land. Damping is small compared to the critical damping of a harmonic oscillator to allow sound waves to travel in the ice, but large enough to hinder build up of vibrational kinetic energy in the ice. Young's modulus $2 \times 10^9 N/m^2$Fracture stress $5 \times 10^{-4} N/m^2$Fracture mode tension + constant*(bending and torsion)Ice density $910kg/m^3$ Water density $1027kg/m^3$DE diameter $8m$Air drag $1Ns/m^3$Water drag $20Ns/m^3$Land friction $10^6 Ns/m^3$Damping/c 10^{-3}~~

3 ~~Numerical examples~~Kvarken region March 2018

3.1 ~~Kvarken region March 2018~~

Kvarken is the narrow and shallow neck between the Bay of Bothnia and the rest of the Gulf of Bothnia. In a typical winter, such as the winter 2018 was, the Bay of Bothnia freezes over completely , while the rest of the Gulf of Bothnia freezes only partly. This makes Kvarken an interesting places for ice dynamics as, with strong Northern or Eastern winds, the sea ice in the Bay of Bothnia is fragmented and pushed through the narrow Kvarken strait. During severe winters, ice arches can develop on

the Northern side of Kvarken. Physically, ice dynamics in Kvarken resembles that of Nares Strait where ice arching is common Moore et al. (2023).

We simulate two different cases of ice dynamics, which occurred on 8 and 23 March 2018. For the simulation domain we use a ~ 100 m resolution digital depth model of the Baltic Sea, freely distributed online by the Baltic Sea Hydrographic Commission, and for comparison with simulation results we use Copernicus-data satellite images from the LandSat program (see data availability below). For forces driving the ice fragmentation we mimic wind directions and magnitudes from weather data archives.

Initially ice is set to cover the entire domain, except for a region south-west of the narrowest part of Kvarken, where we initially have a rectangular area of open water to roughly mimic the ice situation in March 2018. The northern and eastern domain boundaries are fixed, while the southern and western boundaries allow ice to flow out of the domain, except where land is blocking ice motion, obviously. Discrete element diameter is 8 m, and we set the beam width to 40% of the diameter. Further, we introduce disorder and strength variations in the ice by initially reducing the density of beams from its maximum, at uniformly random and uncorrelated locations. We use slightly different setups for ~~different~~ the two cases: The density of the beams is reduced by 40% over the entire domain (23/3/18), and for partly refrozen ice rubble that often appear at open sea we reduce the density of beams by 40%, while fast ice regions in the inner archipelago has zero reduction in beam density (8/3/18). Strength-wise this corresponds to ice that is about ~~1~~ 1.3 m thick.

3.1 23 of March 2018

For 23/3/18, nearby weather stations reported moderate western wind early on the 22 of March, which then strengthened and turned to Northern wind $9 - 11 m/s$, then turned to North-Eastern, and eventually weakened during 23 of March. To model this we applied a constant force, from the north, on all ~~particles~~ elements for 3 hours, followed by 45 minutes of force from the north-east. In this case~~we used the damaged ice with 40% beams missing for~~ , as explained above, the ice is similar over the entire domain. The resulting ice motion is displayed in Fig~~.4~~. 3A, and the largest compressive strains at the end of the simulation in Fig~~.4B. Figure 5A is a~~. 3B. These two figures show clearly the 'bottleneck behaviour' of ice motion through the Kvarken strait. Ice that have passed southwest of the narrowest region move fast, while compressive stresses are built up northeast of the narrowest region leading to reduction of ice speed. Ice is breaking up along compressive shear fracture zones, and some evidences of compressive arches are visible upwind of the narrowest point of the strait. Some additional ice compression, that is not related to ice motion through the strait, is visible at the northern side of the Finnish archipelago.

Figure 3C depicts satellite image of ~~the same region~~ around the Kvarken on 23 of March.~~Figure 5B, shows the corresponding simulated fracture pattern~~Corresponding simulated fracture pattern is shown in Figure 3D. The model derived figure is rendered to mimic the satellite image except for land that is brown so it can easily be distinguished from open water. The similarity between these two images is striking, but there are also some noticeable differences: *(i)* There is significantly more open water east and north of Holmön (marked by 'H' in Fig. 3A). This is most likely due to differences in initial conditions. In the simulations the initial condition was a 100% ice covered Bay of Bothnia, while in the reality there existed a wide lead of open water along the Swedish cost the days before the 23 of March. *(ii)* Ice floes has travelled much further through the Kvarken

Figure 3. (*A*) Color coded ice motion for the 23/3/18 simulation. Dark red correspond to the largest motion, which in this case reaches up to about $4.5km$. 'Swe' and 'Fin' marks the Swedish and Finnish mainlands, respectively. 'H' marks the location of Holmön. (*B*) The largest compressive strains on intact beams connecting DEs at the end of the simulation. (*C*) A satellite image of the Kvarken area on 23/3/18 (S2, LC8/9 & S3, 23.03.2018, from the TARKKA database as described in data availability below). 'T' marks the location of the Torsön Island, 'Ö' the location of the Öuran Island, and 'V' the Valsörarna Island. (~~*B*~~*D*) The simulated fracture pattern after 3 hours and 45 minutes. This image display (with black dots) all beams that are strained more than 5% of their original length (and thereby obviously broken). Water is black, ice is gray, and land brown. (*E*) Fast ice regions extracted from the satellite image for 23/3/18 (S2, LC8/9 & S3, 23.03.2018). (*F*) Fast ice regions at the end of the 23/3/18 simulation. (*G*) Crushed region and tensile cracks marked by 'C' extracted from the satellite image for 23/3/18 (S2, LC8/9 & S3, 23.03.2018). (*H*) Crushed regions and tensile cracks at the end of the 23/3/18 simulation. (*I*) The computed FSD at the end of the 23/3/18 simulation fitted by power-law with exponent 1.76. The scale on the x-axis is number of elements, DEMs, in a floe (1 DEM$\approx 50m^2$)

strait in the satellite image compared to the simulations for which the floes are closer to their original position. The reason for this is simply that the simulation cover 3 hours and 45 minutes of ice motion, while in reality the motion has lasted for about a day.

In the Figures 3E and 3F, the drift and the landfast ice are highlighted in the satellite and simulated images, respectively. Again, the similarities between the two images is striking, but there are also visible differences: The fairly straight south-west north-east lead that marks the boundary between drift and landfast ice goes a bit more to the north in the simulation compared to the satellite image. This lead begins near Valsörarna (marked by 'V' in Fig. 3D) and reach the Finnish coast at the Öuran Island (marked by 'Ö') in the satellite image, and further north near Torsön Island (marked by 'T') in the simulations.

~~(A) Color coded ice motion for the 23/3/18 simulation. Dark red correspond to the largest motion, which in this case reaches up to about $4.5km$. 'Swe' and 'Fin' marks the Swedish and Finnish mainlands, respectively. 'H' marks the location of Holmön. (B) The largest compressive strains on intact beams connecting DEs at the end of the simulation.~~ Figures 3G and 3H highlight regions with highly disintegrated ice adjacent to the boundary between drift ice and landfast ice. The reason why the ice become so much crushed in this region is that it is pressed southwards by the wind, and high compressive forces will therefore appear on the northern side of the Finnish archipelago. The difference in shape and extent of the simulated and observed crushed ice regions are again a consequence of the shorter ice dynamic time in the simulations. A longer simulation would induce more shear crushing against the fast-ice margin as the drift ice slowly move west through the Kvarken strait. Another consequence of this particular dynamics is appearance of east-west tensile stress in the drift ice region. Such stresses are typical for shear zones and often induce tensile cracks, more or less, perpendicular to the shear zone. Such cracks are marked by 'C' in Figs 3G and 3H.

3.2 8 of March 2018

The other date for model testing in the Kvarken region is 8/3/18. During a few days proceeding this ~~date~~ day there was a fairly constant mostly eastern wind. We use the same initial state in this case as for 23/3/18, except that we now define two region

of ~~fast ice . The first region~~ stronger landfast ice to test how this influence the outcome of simulations. One region of stronger ice is the strait between Holmön and the Swedish main land, and the other region is the Finnish archipelago along the southern border of the domain terminating close to Valsörarna (marked by 'V' in Fig. ~~5B). This boundary between strong ice and weak ice become visiblein Fig.3~~3D). The effect this has is visible, for example, in Fig. 2B. The damaged ice breaks, while the fast ice remain solid. ~~Other differences in this simulations is that the force~~ Another differences to the previous case is that now the wind forcing on DEs comes from the east and not the north, and the simulation is a bit shorter ~~. The ice motion and compressive stresses are~~ (3 hours 15 minutes instead of 3 hours 45 minutes).

Ice motion is displayed in Fig. ~~6, and simulated and observed fracture patterns are displayed in Fig. 7.~~

~~(A) Color coded ice motion for the 8/3/18 simulation. Dark red correspond to the largest motion, which in this case reaches about 3.5km. (B) The largest compressive strains on intact beams connecting DEs at the end of the simulation.~~

~~(A) A satellite image of the Kvarken area on 8/3/18 (S2, LC8/9 & S3, 08.03.2018). (B) The simulated fracture pattern after 3 hours and 15 minutes. This image display (with black dots) all beams that are strained more than 5% of their original length (and thereby obviously broken), and beams compressed more 0.02% (light gray dots) of their original length.~~

~~There are many similarities in ice motion and fragmentation between the 8 and 23 March 2018 simulations. This reflects the fact that ice motion in this region is heavily influenced by the topography of the archipelago and the coastlines of Finland and Sweden. The ice is pressed through the Kvarken strait by northern to eastern winds. In both cases the Kvarken strait is a bottleneck and indications of compression arches are seen in Figs. 4B and 6B. The fast ice regions emerging from the 23/3/18 simulation in both the Finnish archipelago and between Holmön and the Swedish cost very closely resembles the satellite images. Notice that this~~ 4A, and the largest compressive strains at the end of the simulation in ~~which we did not explicitly implement fast ice regions in the model. The fast ice regions extracted from the satellite images above are displayed in Fig. 8A, and the corresponding fast ice emerging from the simulations are displayed Fig. 8B. These two figures form a good example of the accuracy of the HiDEM model. There are clear similarities between the observed and the simulated fast ice regions, but there are also easily spotted differences.~~

~~For 23/3/18, the fairly straight south-west north-east lead that marks the boundary between broken and fast ice goes a bit more to the north in the simulation as compared to the satellite image, reaching the Finnish coast at the Öuran Island instead of the Torsön Island. Another difference between observed and simulated ice configurations for the~~ Fig. 4B. Similarly to the 23~~March 2018 case is that there is significantly more open water east and north of Holmön in the observed images. This originates from differences in initial conditions. In the simulations the initial condition was a 100% ice covered Bay of Bothnia, while in the observed case there existed a wide lead of open water along the Swedish cost the days before the 23. This difference is clearly seen in Fig. 5. Finally, as a consequence of the limited time for ice motion in the simulations, the ice floes has not travelled as far through the Kvarken strait in the simulations as in the satellite image.~~

~~For the 8~~/3/18 ~~case there are also many striking similarities between the observed and the simulated ice configurations~~case, ice is pressed through the Kvarken strait, but now the ice comes more from the east than north for obvious reasons. Compressive stress builds up northeast of the strait as in the previous case, but in this case there is also significant compressive fracture of ice against the Swedish coast, as can be seen in Fig. 4B. The ice begin to break up along an east-west corridor ending between

Figure 4. (*A*) ~~Fast~~ Color coded ice ~~regions extracted from~~ motion for the 8/3/18 simulation. Dark red correspond to the largest motion, which in this case reaches about $3.5km$. (*B*) The largest compressive strains on intact beams connecting DEs at the end of the simulation. *C*) A satellite image ~~for 23~~of the Kvarken area on 8/3/18 (S2, LC8/9 & S3, ~~23.03~~08.03.2018). (~~*B*~~*D*) ~~Fast~~ The simulated fracture pattern after 3 hours and 15 minutes. This image display (with black dots) all beams that are strained more than 5% of their original length (and thereby obviously broken), and beams compressed more 0.02% (light gray dots) of their original length. (*E*) Highlighted (light blue) drift ice ~~regions at~~ that is on its way out through the ~~end~~ Kvarken strait. Reddish are cover the land and landfast ice on the eastern (Finnish) side of Kvarken to highlight the ~~23/3/18 simulation~~boundary between drift and fast ice. (~~*C*~~*F*) ~~The computed FSD at the end of~~ Corresponding highlighted regions for the ~~8/3/18~~ simulation~~fitted by power law~~ . 'D' marks the dominante diagonal lead, and 'A' marks cracks formed in regions with ~~exponent 1.72~~compression arches. (~~*D*~~*G*) The computed FSD at the end of the ~~23~~8/3/18 simulation fitted by power-law with exponent ~~1.76~~1.72.

the south-end of Holmön and the Finnish archipelago. The same corridor of fragmented ice can be seen in the satellite image, but in this cases it reaches almost all the way to the Finnish coast. It is quite clear that the simulation would have to run longer for ~~the ice~~ significant fragmentation to reach that far east, even though the ice forcing is slightly exaggerated in the simulations, as explained above.

~~Substantial compressive crushing of sea ice near the Swedish coast is identified in our simulations (Fig. 7B, light gray pattern). Such crushing cannot be detected~~ Figure 4C is the satellite image of the region on 8/3/18. In contrast to the previous case, the simulation image rendered to mimic the observations now displays, as before, fractured beams as black to have the same color as open water, but on top of them all intact compressed beams are rendered as light gray to mimic regions in the satellite image ~~Fig. 7A. This phenomenon~~ that may have densely packed drift ice and would therefore appear white or grayish. It is not possible to determine from the satellite image (Figure 4C) if the regions near the Swedish coast, northeast of Holmön, is densely packed drift, fast ice or something in between. This issue may have two different explanations: ~~The~~ Either the crushing of ice cannot be detected in the satellite image as it does not expose dark open water, or it may ~~indicate that~~ be that the wind forcing was set too strong in the simulations~~in this case~~. The latter is consistent with the weak to moderate eastern winds during 6 to 8 of March. Inspecting satellite images for 6 and 7 of March reveal that it took ~~about~~ at least 3 days to form the east-west fragmentation corridor. Such long times cannot be ~~reached by simulations which could largely explains the differences between observed and simulated.~~ simulated.

Figures 4E and 4F highlight (in light blue) the floes that are about to flow out through the Kvarken strait. In the same figures, reddish areas marks the land and landfast ice on the eastern side of Kvarken. The light blue areas display obvious similarity, and the eastern border between drift ice and landfast ice, indicated by the boundary of the reddish area, are very similar for the observed and the simulated. A dominant diagonal lead, marked by a 'D' appear in both images. The exact locations of this lead differs however a bit between the observed and the simulated. Finally, marked by 'A' there are cracks in both images that have the characteristic curved shape of cracks formed in regions with compression arches.

~~(A) Simulated strain field in the Bay of Riga induced by South Western winds. (B) FSD of the Bay of Riga simulation. (C) Result of a box-counting algorithm for compression ridges, $N(L/l) \propto L/l^D$, where l is box length, L is domain length, and N is the number of boxes containing ridges.~~

Figure 5. (a) HiDEM simulation of a failure of a 10 km $\times$ 10 km square-shaped sea-ice sheet subjected to uniaxial compression. The sheet was modelled by using dense-packed single-layer $1m$-diameter spherical discrete elements. The ice sheet fails in shear and ice ridges are formed. (b) An aerial picture at $30m$ altitude of fractured ice with pressure ridges in the Gulf of Bothnia after a storm in March 2011.

3.3 Floe size distributions

The floe size distribution (FSD) that form in the simulations can be extracted. We were not, however, able to extract the corresponding FSDs from the satellite images. Observed FSDs have recently been published by Denton et al. for the Canada Basin (Denton and Timmermans (2022)). They reported power-law FSDs, $n(s) \propto s^{-\alpha}$, with exponents α ranging from 1.65 to 2.03 over a floe-area range from $50m^2$ to $5km^2$, with the larger exponent values appearing in the summer and autumn, and at low ice coverage. The FSDs from the 8/3/18 and 23/3/18 simulations are displayed in ~~Figs 8C and 8D~~Fig. 4G and Fig. 3I, respectively. Power-laws are evident with exponents 1.72, and 1.76, respectively. Also the size-ranges are similar to those reported by Denton et al. However, the discreteness of the DEM become influential for the smallest floe sizes: a single ~~particle~~ element have an area of $\pi r^2 \approx 50m^2$. As single DEs cannot be broken there is a 'pile up' effect in the FSDs for floes with a single or a few DEs. The largest 'floes' in the FSDs, outside of the power-law range, represent the fast ice regions.

4 Gulf of Riga

An important characteristic of sea ice compression is the formation of pressure ridges. In order to demonstrate how pressure ridges form in HiDEM, a square shaped sea-ice sheet of size 10 km $\times$ 10 km was modelled using DEs of 1m diameter and subjected to uniaxial compression. Figure (5A) shows the outcome of this exercise. Fig. (5B) shows an aerial photograph of ice ridges in the Gulf of Bothnia in March 2011 for comparison. The dynamics process of ridge formation become rather evident in these two images. Compression, induced by a strong wind, breaks up the ice in floes. Along the floe boundaries the ice fractures in compressive shear zones and ice rubble builds up to form ridges. In the simulated image, the floes still remain largely at their original position in relation to each other, while in Fig. (5B) they have moved enough to form patches of open water between them.

4.1 ~~Bay of Riga~~

~~To demonstrate the influence of coastal topography we have included a simulation of sea-ice in the Northern part of the Bay of Riga~~Pressure ridge formation is a particular hindarance for shipping in Baltic Sea. In the Gulf of Riga, ridges typically form under compression from ~~a South-western wind. This configuration is~~ southwestern winds. Such conditions are known to produce ~~compression ridges~~ridges, in particular between the Kihnu and Saaremaa islands. The strains between DEs, that

Figure 6. (*A*) Simulated strain field in the Gulf of Riga induced by South Western winds. (*B*) FSD of the Gulf of Riga simulation. (*C*) Strain rate distribution, $n(e)$, of the largest strains, e, in the Gulf of Riga simulation.

were initially connected by beams, at the end of ~~the simulation~~ a simulation of this region are displayed in Fig. ~~9A (that is, both~~ 6A. Both intact and broken beams are included~~)~~. Formed compression ridges appear in the figure as vague red bands of tension in an otherwise compressive ice landscape. The FSD extracted from the ~~Bay~~ Gulf of Riga simulation is displayed in Fig. ~~9B~~6B. The exponent in this case is significantly larger ($\alpha \approx 2.12$) compared to the Kvarken simulations. This is consistent with the fact that the topography of the ~~Bay~~ Gulf of Riga does not allow for ice to flow out of the domain in contrast to the Kvarken strait, and therefore the ice floes are crushed and grinded to smaller sizes (Sulak et al. (2017); Åström et al (2021)). The strain-rate distribution can be extracted from the same data as in Fig.6A. For the largest strains the distribution of rates (Fig. 6C) is consistent with power-law distributions observed at much larger scales (Girard et al. (2009)).

~~At the moment we do not have observational data for ridge patterns~~

To further investigate ridge formation in the Gulf of Riga we identify locations of compression ridges in the simulations as places where elements are pressed below the sea surface to form ridge keels. Ridges are displayed as blue dots together with the bathymetry in Fig. 7A. It is ~~, however,~~ evident from this figure that when long ridges are formed in a single event, like in our simulations, the structure of the ridges is strongly influenced by the shape of the coast line and the bathymetry in shallow waters where ridge keels begin to get grounded. It is therefore reasonable to expect that ridge patterns form fractals~~as so many other~~, just like coastlines and many structures formed by dynamics sea ice (Weiss (2001)) ~~. We identified simulated ridge patterns by locations of DEs pressed below the ice surface to form ridge keels~~do. A simple box counting algorithm, $N(L/l) \propto L/l^D$ ~~then revealed their~~ can reveal the fractal dimension D. Here L/l is the linear number of boxes the domain is divided into, and N is the number of boxes containing DEs identified as ridge keels. Fig. ~~9C~~ 7B shows the result of this exercise, ~~and reveal~~ which indicate that $D \approx 1.12$, which is a fairly low dimension. $D = 1$ would mean that ridges form non-fractal linear structures. It is reasonable to expect that if ridge fields were formed over longer periods and by different wind directions they could eventually cover entire areas, and their dimension would then become $D = 2$. ~~It is also evident from Fig.8A that when long ridges are formed in a single event, like in our simulations, the structure of the ridges is influenced by the shape of the coast line and the bathymetry in shallow waters where ridge keels begin to get grounded.~~ The fractal dimension $D = 1.12$ is a rather typical value for reasonably straight coastlines like in the ~~Bay~~ Gulf of Riga. ~~The location of ridges~~

Fig. 7C shows locations of ice ridges observed from ice charts during 2000-2016. The ridge locations follow reasonably well the general ridge pattern of the simulations indicated by the reddish area in Fig. 7C. Fig. 7D shows the wind statistics (i.e. a wind rose) from the ERA5 dataset (location 58.00 and 23.75) for the same time (December 15th until May 1st in ~~relation to shallow water bathymetry is explicitly displayed in Fig. 10.~~ 2000-2016). This figure demonstrate that ridges are predominantly caused by SW winds, which is the dominant direction of strong winds in the area.

Figure 7. (*A*) Color coded bathymetry. The water surface is at 57m. Locations of DEs that make up compression ridges are indicated by blue markers. Single DEs ~~begin to get~~ on the surface would become grounded in dark red areas. Gray is land. Axis are in meters. (*B*) Result of a box-counting algorithm for compression ridges, $N(L/l) \propto L/l^D$, where l is box length, L is domain length, and N is the number of boxes containing ridges. (*C*) Observed locations (lon,lat) of ridges from ice charts. The statistics is based on the data from winters 2000-2016 (15 December - 1 May). Red stars are ridge locations, and the diameter of the black circles indicates the number of days of ridged ice at that location. The reddish region outline the area where ridges form in the simulations (*D*) A windrose of winds greater than 0, 10 and 15 m/s for December 15th until May 1st, 2000-2016. Frequency intervals for the dashed lines is 10%.

5 Discussion

The results reported here in combination with earlier results on ice shelf disintegration (Benn et al. (2022)), lab-scale ice crushing experiments (Prasanna et al. (2022)), and glacier calving (Åström et al (2021)) demonstrate that HiDEM is capable of simulating the physics of ice fragmentation. In principle, it is possible to use the code in its current form to predict sea ice motion and fragmentation for a few days over length scales of a few hundred kilometers. In order to obtain a constant supply of high-fidelity forecast it would however demand a procedure to obtain high quality assessment of initial conditions. Not only would it demand a detailed knowledge of variations in ice thickness, but also in ice quality. Also the spatial variations in ice surface roughness would be important as it affects the local stress on the ice applied by wind and current. Furthermore, a detailed forecast of winds and currents would be needed in order to determine the forcing on the ice during the simulations. Finally, it would be important to set proper boundary conditions for each case. In particular, if the ice is allowed to move out of the simulation domain. In case the domain is limited by land this is trivial to assess, but if the domain boundary crosses water with dynamic ice both inside and outside the domain, the situation becomes more difficult.

Further development of the HiDEM code would greatly benefit from improved comparisons with quantitative observational data of sea ice dynamics that could be directly compared to simulation data for any given location. For example: the dynamic development of the floe size distribution, floe shapes, and floe locations for a particular time period in the Kvarken strait would be extremely valuable to further test HiDEM. Similarly, the dynamic formation of compression ridges and ice motion in the Gulf of Riga e.g. during a midwinter storm with SW winds would be equally valuable. Almost any type of observed distribution function, velocity field or stress field of this kind would be useful for comparison with simulations results, as long as the simulation can be initiated by accurate enough initial conditions, and the simulated ice dynamics is driven by valid forcing.

A complicating factor for simulations of this kind, ~~are~~ is the huge difference between the short time-step needed for accurate fracture dynamics, and the relevant time scales for sea ice dynamics. The time resolution, dt, should be smaller than the time it takes for sound to travel across a DE, which for ice means $dt < DE_{diameter}/\sqrt{K + 3G/4} \approx 0.0025sec$, where K is bulk modulus, and G is shear modulus for ice. We use here a time step $dt = 0.001sec$. This means that 3.6 million time steps are needed to simulate 1 hour of ice dynamics. Even for the highly optimized HiDEM code, reasonable simulation times are limited to roughly between a few hours up to a few tens of hours, depending on available compute resources. In contrast, the

relevant time scale for sea-ice dynamics may be days, weeks and months. It is, however, possible to speed up ice dynamics in the simulations a bit compared to the pace in nature.

The limitation in simulation times means that entire winter seasons of sea-ice dynamics cannot reasonably be computed. Instead a sea-ice snapshot in time has to be created based on observations and the near-future ice dynamics may then be computed from such a starting point.

It should be noticed that the HiDEM code only simulates sea ice dynamics as elastic-brittle fracture and dynamics. An important aspect that is missing is the thermodynamic processes involved in sea ice formation and disintegration. Ice may, obviously, disintegrate by melting and water may freeze to form new ice or freeze together ice blocks within drift ice. Over long periods of time and in very warm or very cold conditions the thermodynamic processes easily become dominant for sea ice behaviour, while e.g. during short periods of time, in which ice is exposed to stresses that exceed its strength, elastic-brittle behaviour often become dominant. The best way to model the entire range of processes would likely be to combine a code like HiDEM with large scale continuum models that include modelling of thermodynamic processes. For the specific days investigated here (23/3/18 and 8/3/18) the air temperature in Kvarken varied around -10 ° C, which would indicate that some formation of new ice was taking place, but because of the fairly windy conditions the effect would still have been rather marginal over the time scale of a few tens of hours relevant for elastic-brittle breakup.

6 Conclusions

Here we have applied the HiDEM model to sea ice fragmentation and demonstrated that it can ~~reproduce rather well~~ rather well reproduce observed features. The fracture patterns and ice motion resembles those observed ~~via~~ in satellite images. Floe size distributions and compression ridge formations also coincide with observations. As an operational forecast model there are however limitations to the usefulness of the code. The domains possible to simulate with a high resolution are limited in size. Also the duration of the simulated ice dynamics is limited. In contrast, the model gives very high resolution results of fractures, leads, compression ridges, and floes. It seems that the best way forward for ice dynamics forecasts would be a combination of DEM and continuum models.

Code and data availability. A release version of HiDEM is available at https://doi.org/10.5281/zenodo.1252379. The bathymetry for the simulations are provided by the Baltic Sea Hydrographic Commission freely available at: http://data.bshc.pro. The satellite images are: ESA Copernicus Sentinel Data SYKE (2018), and USGS/NASA Landsat program SYKE (2018), provided by the Finnish Environment Institute SYKE, available at: https://wwwi4.ymparisto.fi/i4/eng/tarkka.

Author contributions. The authors FR and JÅ have constructed the HiDEM code. JÅ set up the simulations, performed them, analysed the results and has written parts of the paper. JH and AP contributed to analysis of the model results and writing of the manuscript. RU and IM contributed the observational data for the Gulf Riga and participated in writing of the manuscript.

Competing interests. At least one of the (co-)authors is a member of the editorial board of The Cryosphere.

Acknowledgements. This work was supported by the NOCOS DT project funded by the Nordic Council of Ministers. JH and AP acknowledges the financial support from the Research Council of Finland research project (348586) WindySea - Modelling engine to design, assess environmental impacts, and operate wind farms for ice-covered waters.

References

Åström, J.A., Benn, D.I.: Effective rheology across the fragmentation transition for sea ice and ice shelves, Geophysical Research Letters, 46, 22, 13099-13106, 2019

Åström, J.A., Cook, S., Enderlin, E.M., Sutherland, D.A., Mazur, A., Glasser, N: Fragmentation theory reveals processes controlling iceberg size distributions, Journal of Glaciology, 67, 264, 603-612, 2021

Åström, J.A., Riikilä, T.I, Tallinen, T., Zwinger, T., Benn, D.I., Moore, J.C., Timonen, J.: A particle based simulation model for glacier dynamics, The Cryosphere, 7, 5, 1591-1602, 2013

Babic, M., Shen, H., Bedov, G.:Discrete element simulations of river ice transport. InProc.of the 12th IAHR Int. Symposium on Ice, 1, 564–574, Espoo, Finland, 1990

Benn, D.I., Åström, J.A.: Calving glaciers and ice shelves, Advances in Physics: X, 3, 1, 1513819, 2018.

Benn, D. I., Luckman, A., Åström, J.A., Crawford, A.J., Cornford, S.L., Bevan, S.L., Zwinger, T., Gladstone, R., Alley, K., Pettit, E., Bassis, J.: Rapid fragmentation of Thwaites Eastern Ice Shelf, The Cryosphere, 16, 6,, 2545-2564, 2022

Blockley, E. at al. : The future of sea ice modelling. Toward defining a cutting-edge future for sea ice modelling: An International workshop, Laugarvatn, Iceland, 23-26 September 2019, Bulletin of American Meterological Society, E1304, 2020

Bouchat, A.: Sea Ice Rheology Experiment (SIREx): 1. Scaling and Statistical Properties of Sea-Ice Deformation Fields, Journal of Geophysical Research: Oceans, 127, 4https://doi.org/10.1029/2021JC017667, 2022

Damsgaard, A., Adcroft, A., Sergienko, 0.: Application of Discrete Element Methods to Approximate Sea Ice Dynamics. Journal of Advances in Modeling Earth Systems, 9, 2228-2244, 2018

Damsgaard, A. and Sergienko, O., Adcroft, A.: The Effects of Ice Floe-Floe Interactions on Pressure Ridging in Sea Ice, Journal of Advances in Modeling Earth Systems, 13, e2020MS002336, 2021

Dansereau, V., Weiss, J., Saramito, P., and Lattes, P.: A Maxwell elasto-brittle rheology for sea ice modelling, The Cryosphere, 10, 1339–1359, https://doi.org/10.5194/tc-10-1339-2016, 2016

Denton, A. A., Timmermans, M-L: Characterizing the sea-ice floe size distribution in the Canada Basin from high-resolution optical satellite imagery, The Cryosphere, 16, 1563–1578, 2022.

Girard, L., Weiss, J., Molines, J. M., Barnier, B., Bouillon, S.: Evaluation of high resolution sea ice models on the basis of statistical and scaling properties of Arctic sea ice drift and deformation, Journal of Geophysical Research, 114, C08015. https://doi.org/10.1029/2008JC005182, 2009

Hibler, W.D.I.: A viscous sea ice law as a stochastic average of plasticity, J. Geophys. Res., 82, 3932–3938, 1977

Hibler, W.D.I.: A dynamic thermodynamic sea ice model, J. Phys. Oceanogr., 9, 815–846, 1979

Hutter, N.: Sea Ice Rheology Experiment (SIREx): 2. Evaluating Linear Kinematic Features in High-Resolution Sea Ice Simulations,Journal of Geophysical Research,127,4https://doi.org/10.1029/2021JC017666, 2022

Hopkins, M., Hibler, III WD: Numerical simulations of a compact convergent system of ice floes. Ann. Glaciol., 15, 26–30. (doi:10.1017/S0260305500009502), 1991

Hopkins, M., and Thorndike, A. S.: Floe formation in Arctic sea ice, Journal of Geophysical Research: Oceans, 111, C11, 2006

Kärnä, T., Ljungemyr, P., Falahat, S., Ringgaard, I., Axell, L., Korabel, V., Murawski, J., Maljutenko, I., Lindenthal, A., Jandt-Scheelke, S., Verjovkina, S., Lorkowski, I., Lagemaa, P., She, J., Tuomi, L., Nord, A., and Huess, V.: Nemo-Nordic 2.0: operational marine forecast model for the Baltic Sea, Geosci. Model Dev., 14, 5731–5749, https://doi.org/10.5194/gmd-14-5731-2021, 2021.

Manucharyan, G. E., and Montemuro, B. P.: SubZero: A sea ice model with an explicit representation of the floe life cycle, Journal of Advances in Modeling Earth Systems, 14, e2022MS003247, 2022

Acheson, D. J.: Elementary Fluid Dynamics. Oxford University Press. p. 205. ISBN 0-19-859679-0, 1990

Meyers, M. A., and Chawla, K. K.: Mechanical behavior of Materials, 570–580. Prentice Hall, Inc. 2009

Moore, G.W.K., Howell, S.E.L. & Brady, M. Evolving relationship of Nares Strait ice arches on sea ice along the Strait and the North Water, the Arctic's most productive polynya. Sci Rep 13, 9809 (2023). https://doi.org/10.1038/s41598-023-36179-0

Ólason, Einar and Boutin, Guillaume and Korosov, Anton and Rampal, Pierre and Williams, Timothy and Kimmritz, Madlen and Dansereau, Véronique and Samaké, Abdoulaye: A New Brittle Rheology and Numerical Framework for Large-Scale Sea-Ice Models, Journal of Advances in Modeling Earth Systems,14,8, https://doi.org/10.1029/2021MS002685,

Pemberton, P., Löptien, U., Hordoir, R., Höglund, A., Schimanke, S., Axell, L., and Haapala, J.: Sea-ice evaluation of NEMO-Nordic 1.0: a NEMO–LIM3.6-based ocean–sea-ice model setup for the North Sea and Baltic Sea, Geosci. Model Dev., 10, 3105–3123, https://doi.org/10.5194/gmd-10-3105-2017, 2017.

Polojärvi, A.: Numerical model for a failure process of an ice sheet, Computers & Structures 269, 106828, 2022

Prasanna, M., Polojärvi, A, Wei, M., Åström, J.: Modeling ice block failure within drift ice and ice rubble, Physical Review E 105 (4), 045001, 2022

Riikilä, T.I., Tallinen, T., Åström, J.A., Timonen, J.: A discrete-element model for viscoelastic deformation and fracture of glacial ice, Computer Physics Communications 195, 14-22, 2015

Röhrs, J., Gusdal, Y., Rikardsen, E., Duran Moro, M., Brændshøi, J., Kristensen, N. M., Fritzner, S., Wang, K., Sperrevik, A. K., Idžanović, M., Lavergne, T., Debernard, J., and Christensen, K. H.: Barents-2.5km v2.0: An operational data-assimilative coupled ocean and sea ice ensemble prediction model for the Barents Sea and Svalbard, Geosci. Model Dev. Discuss. [preprint], https://doi.org/10.5194/gmd-2023-20, in review, 2023.

Schreyer, H.L., Sulsky, D.L., Munday, L.B., Coon, M.D., and Kwok, R.: Elastic-decohesive constitutive model for sea ice, J. Geophys. Res., 111, C11S26, doi:10.1029/2005JC003334, 2006

Sulak, D. J., Sutherland, D. A., Enderlin, E. M., Stearns, L. A., and Hamilton, G. S.: Iceberg properties and distributions in three Greenlandic fjords using satellite imagery, Annals of Glaciology, 58. https://doi.org/10.1017/aog.2017.5, 2017

Tuhkuri, J., Polojärvi, A.: A review of discrete element simulation of ice–structure interaction, Phil.Trans.R.Soc.A376: 20170335.http://dx.doi.org/10.1098/rsta.2017.0335, 2018

Weiss, J.: Fracture and fragmentation of ice: a fractal analysis of scale invariance. Engineering Fracture Mechanics, 68(17-18), 1975–2012, 2001

West, B., O'Connor, D., Parno, M., Krackow, M., and Polashenski, C.: Bonded discrete element simulations of sea ice with non-local failure, Applications to Nares Strait. Journal of Advances in Modeling Earth Systems, 14, e2021MS002614, 2022

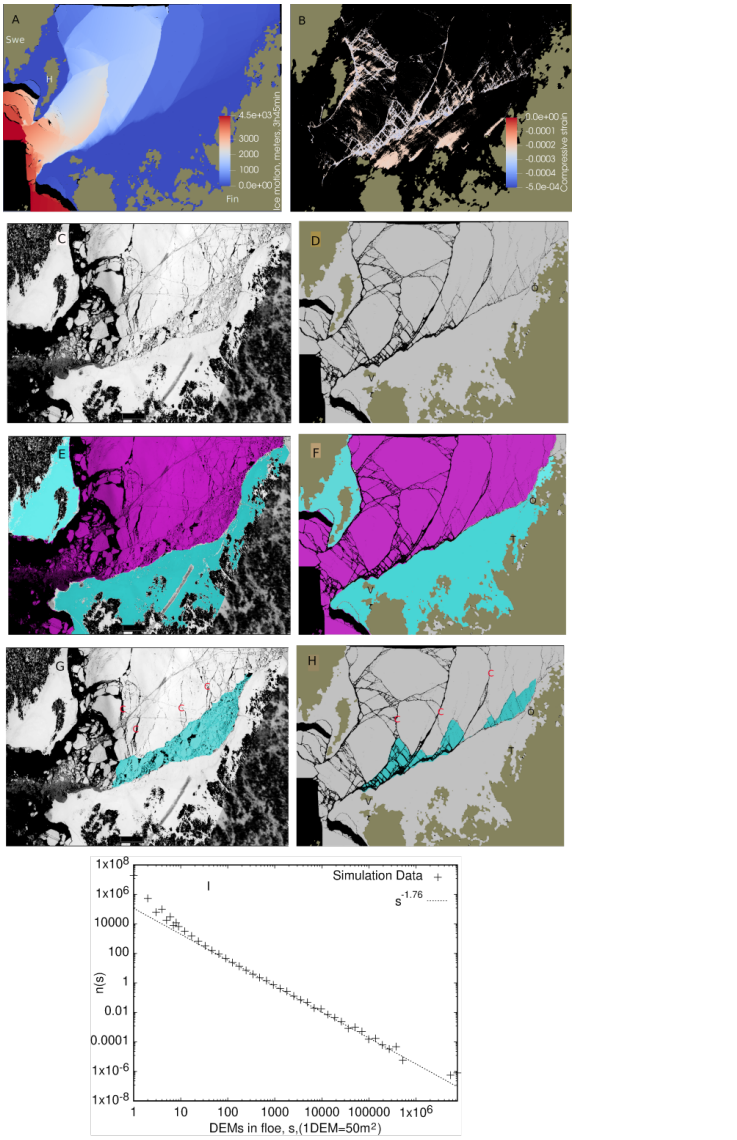

Figure 3. (*A*) Color coded ice motion for the 23/3/18 simulation. Dark red correspond to the largest motion, which in this case reaches up to about $4.5km$. 'Swe' and 'Fin' marks the Swedish and Finnish mainlands, respectively. 'H' marks the location of Holmön. (*B*) The largest compressive strains on intact beams connecting DEs at the end of the simulation. (*C*) A satellite image of the Kvarken area on 23/3/18 (S2, LC8/9 & S3, 23.03.2018, from the TARKKA database as described in data availability below). 'T' marks the location of the Torsön Island, 'Ö' the location of the Öuran Island, and 'V' the Valsörarna Island. (*D*) The simulated fracture pattern after 3 hours and 45 minutes. This image display (with black dots) all beams that are strained more than 5% of their original length (and thereby obviously broken). Water is black, ice is gray, and land brown. (*E*) Fast ice regions extracted from the satellite image for 23/3/18 (S2, LC8/9 & S3, 23.03.2018). (*F*) Fast ice regions at the end of the 23/3/18 simulation. (*G*) Crushed region and tensile cracks marked by 'C' extracted from the satellite image for 23/3/18 (S2, LC8/9 & S3, 23.03.2018). (*H*) Crushed regions and tensile cracks at the end of the 23/3/18 simulation. (*I*) The computed FSD at the end of the 23/3/18 simulation fitted by power-law with exponent 1.76. The scale on the x-axis is number of elements, DEMs, in a floe (1 DEM$\approx 50m^2$)

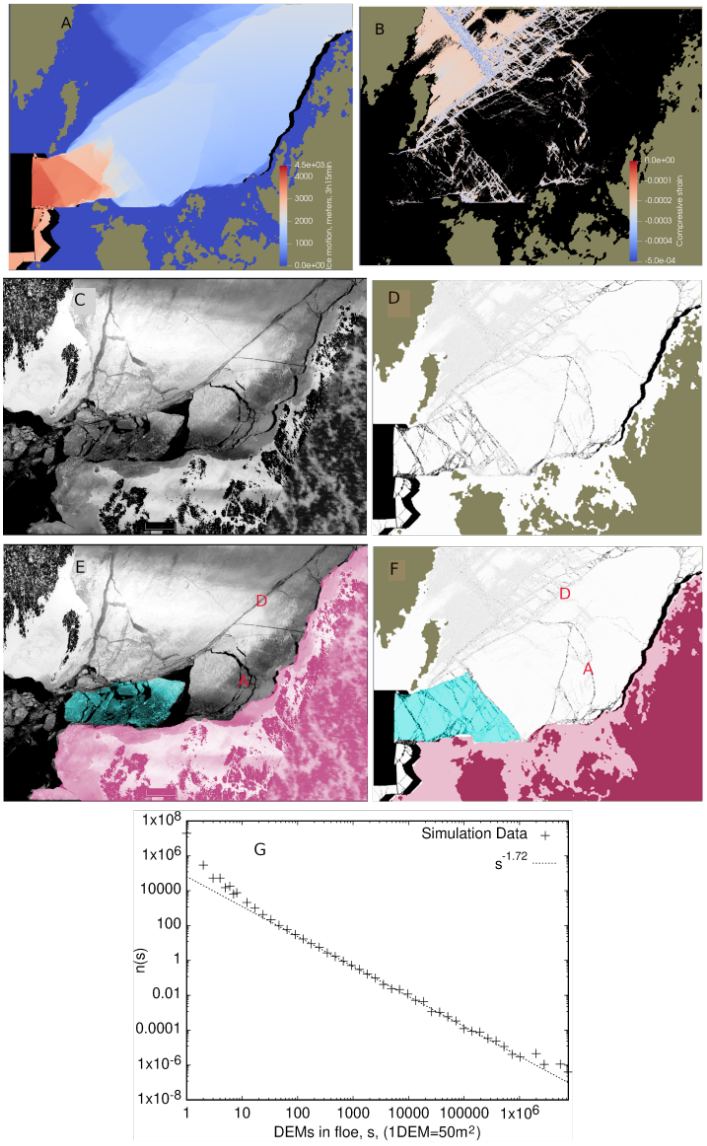

Figure 4. (*A*) Color coded ice motion for the 8/3/18 simulation. Dark red correspond to the largest motion, which in this case reaches about $3.5km$. (*B*) The largest compressive strains on intact beams connecting DEs at the end of the simulation. *C*) A satellite image of the Kvarken area on 8/3/18 (S2, LC8/9 & S3, 08.03.2018). (*D*) The simulated fracture pattern after 3 hours and 15 minutes. This image display (with black dots) all beams that are strained more than 5% of their original length (and thereby obviously broken), and beams compressed more 0.02% (light gray dots) of their original length. (*E*) Highlighted (light blue) drift ice that is on its way out through the Kvarken strait. Reddish are cover the land and landfast ice on the eastern (Finnish) side of Kvarken to highlight the boundary between drift and fast ice. (*F*) Corresponding highlighted regions for the simulation. 'D' marks the dominante diagonal lead, and 'A' marks cracks formed in regions with compression arches. (*G*) The computed FSD at the end of the 8/3/18 simulation fitted by power-law with exponent 1.72.

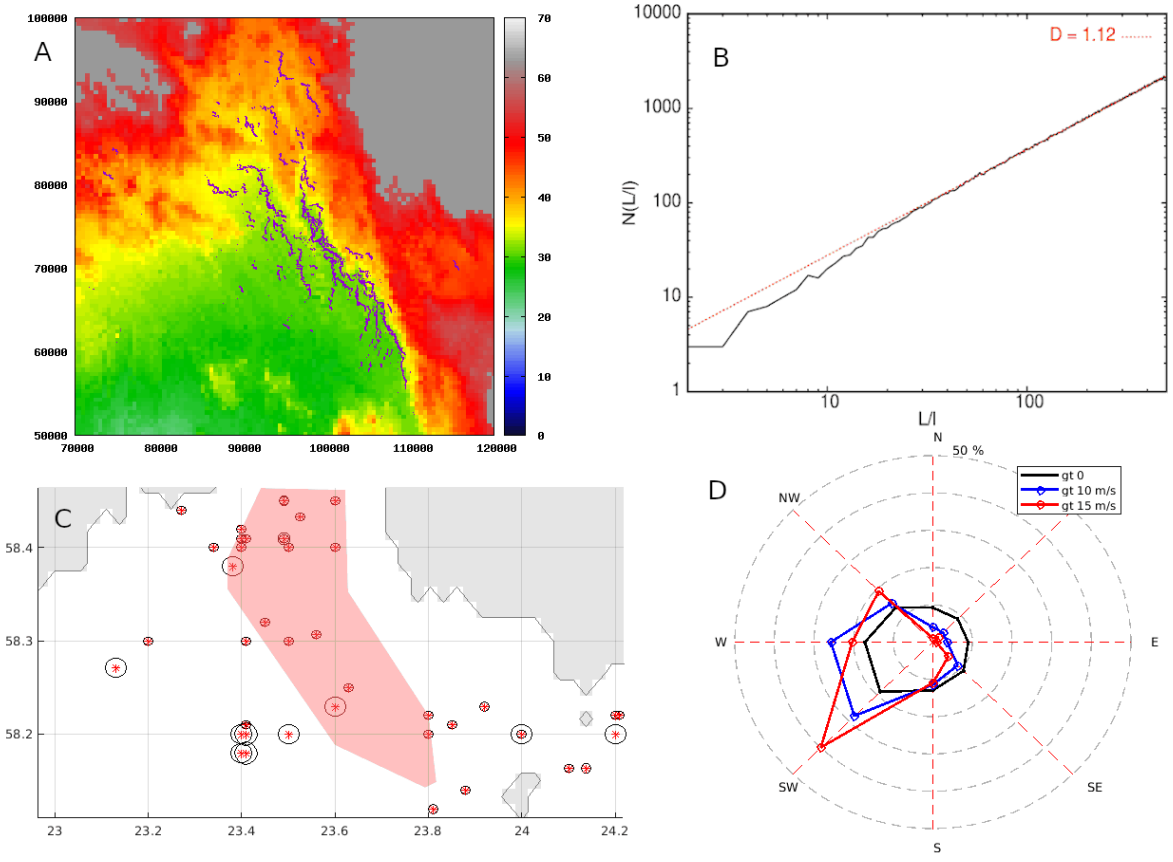

Figure 7. (*A*) Color coded bathymetry. The water surface is at 57m. Locations of DEs that make up compression ridges are indicated by blue markers. Single DEs on the surface would become grounded in dark red areas. Gray is land. Axis are in meters. (*B*) Result of a box-counting algorithm for compression ridges, $N(L/l) \propto L/l^D$, where l is box length, L is domain length, and N is the number of boxes containing ridges. (*C*) Observed locations (lon,lat) of ridges from ice charts. The statistics is based on the data from winters 2000-2016 (15 December - 1 May). Red stars are ridge locations, and the diameter of the black circles indicates the number of days of ridged ice at that location. The reddish region outline the area where ridges form in the simulations (*D*) A windrose of winds greater than 0, 10 and 15 m/s for December 15th until May 1st, 2000-2016. Frequency intervals for the dashed lines is 10%.